Diurnal Variability of Regional Cloud and Clear-Sky Radiative Parameters Derived from GOES Data. Part III: November 1978 Radiative Parameters

PATRICK MINNIS AND EDWIN F. HARRISON

Atmospheric Sciences Division, NASA Langley Research Center, Hampton, VA 23665

(Manuscript received 8 November 1982, in final form 21 February 1984)

ABSTRACT

The diurnal variability of the radiation emitted and reflected from the earth–atmosphere is investigated at the regional scale using November 1978 GOES-East visible and infrared data and GOES-derived cloud information. Narrowband GOES data are converted to broadband radiances using spectral calibration functions determined empirically from colocated Nimbus-7 ERB and GOES-East measurements over ocean, land and cloud surfaces. Shortwave radiances are used to estimate radiant exitances with bidirectional reflectance models derived from GOES and aircraft data for ocean, land and clouds.

Average albedo over clear ocean and land changed by factors of 4.2 and 2.2, respectively, for a solar zenith angle range of 0 to 80°. Average cloud albedo changed by a factor of 1.8 for the same range of solar zenith angles, but varied considerably from region to region. Mean clear-sky longwave radiant exitance varied diurnally from 2 W m^{-2} over some ocean areas to 100 W m^{-2} in one high elevation desert area in the Andes. In some regions having regular deep convective diurnal cycles, the mean cloud longwave flux had a diurnal range as high as 50 W m^{-2}. The mean difference in net radiation between cloudy and clear areas was −55 W m^{-2}, indicating that the clouds had a net cooling effect for the GOES-East viewing area during this time period.

Monthly mean Earth radiation budget (ERB) measurements from Sun-synchronous satellites were simulated to estimate the magnitude of the errors which would result from limited local time sampling of the resultant radiation field. It was found that the monthly mean regional longwave flux could be estimated with a precision better than 3 W m^{-2}. The precision in estimated regional albedo ranged from 1.5 to 4.0% for averaging which uses directional reflectance models and from 2.6 to 11.1% for simple averaging which is dependent on equatorial crossing time. For simple averaging, regional net radiation errors ranged from 10 to 40 W m^{-2} with "global" bias errors as high as 36 W m^{-2} depending on the satellite equatorial crossing time. Similarly, monthly mean regional net radiation errors ranged from 6 to 14 W m^{-2} with "global" bias errors of up to 7 W m^{-2} when directional reflectance models were used.

1. Introduction

Earth radiation budget measurements have been made with a single satellite having either variable local hour coverage for a limited latitudinal range (mid-inclined orbit) or global coverage with fixed local hour coverage (Sun-synchronous orbit). The Tiros IV satellite (Vonder Haar, 1968) flown between ±50° latitude is an example of the former. Nimbus 6 (Jacobowitz *et al.*, 1979) is typical of the latter, the configuration used most frequently for ERB measurements in the last decade. Global coverage is essential for deriving climatological parameters from ERB data. However, it has been noted by most ERB researchers (e.g., Vonder Haar, 1968; Raschke *et al.*, 1973) who have analyzed data from Sun-synchronous satellites that there may be considerable error in the derived radiative quantities due to limited local hour coverage. The largest sampling errors would result primarily from variations in cloudiness which are fairly regular on a diurnal basis.

At present, the magnitude of the sampling errors due to diurnal variability of the viewed-scene meteorology, especially cloud cover, is essentially unknown. Minnis and Harrison (1984b), hereafter referred to as MHb, showed that the mean diurnal variations in cloud cover were significant in many parts of the area viewed by the eastern Geostationary Operational Environmental Satellite (GOES-East) during November 1978. Such variability in cloud amount and cloud height and thickness suggests that the radiation field also has a significant diurnal component over and above that determined by the diurnal cycles of incoming solar radiation and the directional reflectance properties of a static scene. To gain some insight into the impact of diurnal variability on past ERB estimates and to better account for it in future measurement systems, it is necessary to determine the magnitude and temporal and spatial extent of diurnal variations in the Earth's radiation field.

In this paper, the November 1978 cloudiness, visible brightness and thermal infrared data derived by Minnis and Harrison (1984a) (hereafter referred to as MHa) from GOES-East measurements will be

used to estimate the hourly radiation field at the top of the atmosphere. The influence of cloud cover on the ERB will then be evaluated from the cloudiness and resultant radiation data for the time period. The results will also be utilized to assess the sampling errors in monthly mean ERB parameters resulting from measurement of this radiation field with a Sun-synchronous satellite.

2. Methodology

Several steps are necessary to derive broadband shortwave and longwave irradiances from GOES-derived, mean regional infrared window (IR) equivalent blackbody temperature T, visible (VIS) brightness counts D and areal cloud fraction C. First, the IR temperatures and VIS counts must be converted to broadband longwave L_{lw} and shortwave L_{sw} radiances respectively. These radiances are then used with the appropriate anisotropic corrections to compute longwave M_{lw} and shortwave M_{sw} radiant exitances (fluxes) through integration over the upward hemisphere. This section describes derivations of the spectral transformation functions used to accomplish the first step. Bidirectional reflectance models are also derived here in order to facilitate the second step. Directional reflectance is derived from M_{sw} and used to compute the albedo over a given time period. Time-averaged longwave radiant exitance is also found. The albedo and average M_{lw} are then used to compute net radiation gained or lost from a given region. These same quantities are then computed from samples of these monthly mean hourly data taken with ideal Sun-synchronous satellites. Finally, monthly averages of the radiation quantities from the Sun-synchronous cases are compared to the fully sampled case to estimate the monthly mean errors due to limited sampling.

a. Narrowband-to-broadband transformations

A number of previous estimates of the ERB have been derived from radiances measured within relatively narrow spectral ranges. Raschke *et al.* (1973) used a theoretical regression equation and a set of spectral radiances measured with the Nimbus 3 Medium Resolution Infrared Radiometer to compute the broadband longwave (LW) flux. Gruber and Winston (1978) estimated M_{lw} from infrared window (10.5–12.5 μm) measurements taken with a scanning radiometer flown aboard National Oceanic and Atmospheric Administration (NOAA) operational spacecraft. They used a regression fit of window and broadband fluxes derived with a radiative transfer model to estimate M_{lw}. To determine shortwave albedo, they assumed that reflectance in the VIS (0.5–0.7 μm) region is equivalent to broadband (0.2–4.0 μm) shortwave (SW) reflectance.

A different approach is taken here since the Nimbus 7 (N7) ERB (Vonder Haar *et al.*, 1981) instrument was operational during the latter half of November 1978—a primary reason for the selection of GOES data during this time. The N7 scanning radiometer had the capability of viewing a given earth scene several times from different angles during a pass of the satellite. This instrument configuration provided simultaneous views of certain locations with both the GOES-VISSR (Visible and Infrared Spin Scan Radiometer) and the N7 broadband radiometer from the same direction. Thus, it is possible to derive empirical relationships between corresponding spectral and broadband radiances.

Nimbus 7 ERB LW (4.5–50.0 μm) and SW (0.2–4.8 μm) scanning radiometer data were matched with GOES IR window (10.5–12.5 μm) and VIS (0.55–0.75 μm) measurements of approximately the same scene taken within 15 minutes of each other. Colocated data measured at solar zenith ζ, satellite zenith θ and relative azimuth ψ angles were used which satisfied the following constraints:

$$|\zeta - \zeta_7| < 2.5°; \quad |\theta - \theta_7| < 7.5°; \quad |\psi - \psi_7| < 15.0°,$$

where the subscript refers to the N7 scanner, no subscript refers to GOES, and the forward scattering direction is at $\psi = 180°$. Data used in the correlations consisted of single N7 radiances and mean squared VIS counts D^2 and mean equivalent Planck 11.5 μm radiances $BB(T)$, computed from the GOES data within an area defined by the N7 scanner field of view. For the GOES data, this field of view was approximated by a 90 km square centered at the latitude and longitude of the N7 measurement. A sample of 1629 measurement sets over ocean and 501 sets over land met the angular constraints for data taken on 16–30 November 1978. Correlations and multiple regression fits were determined for both LW–IR and SW–VIS data over ocean and land. Most land regions are brighter at longer and shorter wavelengths than they are in the 0.55–0.75 μm region (e.g., Kriebel, 1978). Data from aircraft measurements (NASA, 1971) indicate that clouds reflect the entire solar spectrum more uniformly than other surfaces and have a maximum reflectance within the visible channel range. Oceans are also relatively uniform reflectors, but have a peak albedo around 0.51 μm.

It was found that a quadratic regression fit produced the highest correlation coefficient, 0.96 over both surface types, between the SW and VIS radiances. These relationships for ocean and land are

$$L_{sw} = 1.36(D^2 - 6.25)^{0.5} + 0.0764(D^2 - 6.25), \quad (1a)$$

$$L_{sw} = 1.92(D^2 - 6.25)^{0.5} + 0.0616(D^2 - 6.25), \quad (1b)$$

respectively, for conditions when $D^2 < 1450$. When $D^2 \geq 1450$, a single linear fit,

$$L_{sw} = 28.3 + 0.0923D^2, \quad (2)$$

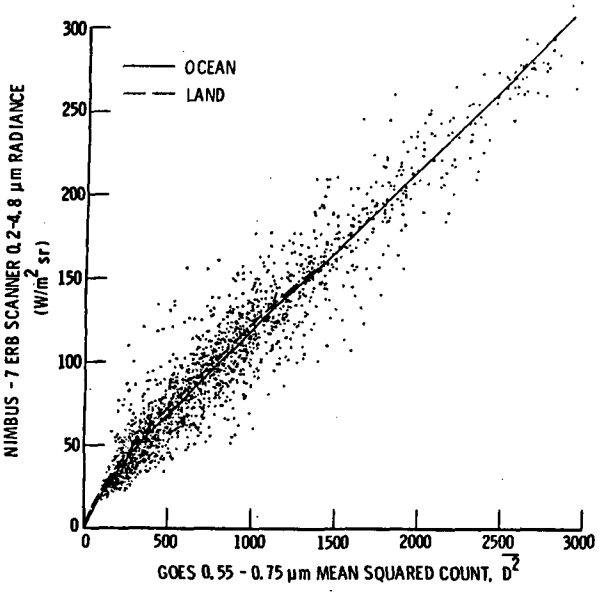

FIG. 1. Correlation of GOES-2 visible and Nimbus 7-ERB broadband shortwave data during November 1978. Curves represent regression fits to the data.

is used over either surface type. This curve was derived for mostly cloudy conditions. The threshold value of D^2 which dictates use of (2) is the value where L_{sw} is the same for both (1a) and (1b). These curves are shown in Fig. 1 with the sample data. The overall root-mean-square (rms) error for all of the regression fits is 14%. The scatter observed in the figure may arise from a number of sources. A large source of error may reside in the colocation of the fields of view and the allowed angular difference between the two satellites. Although the accepted data were constrained to $\theta < 70°$, there were several measurements taken at $50° < \theta < 70°$. For GOES, an error in the location of one pixel, nominally ±8 km, becomes ±16 km, or ±18% of the field of view at $\theta = 60°$. Another large source of scatter may be the use of a single 1 km VIS pixel to represent an 8 km area. Minnis and Harrison (1984a) found that the rms error in the mean VIS brightness for a 250 × 250 km^2 region is 0.4 counts when that type of sampling is used to represent the full 8 km field of view. It is likely that the error in mean VIS brightness will be greater than 0.4 counts for a 90 × 90 km^2 region. An azimuth angle measured relative to the sun permits viewing of a scene from two sides at the same set of angles. Thus, there may be cases where GOES viewed from one side of a scene and N7 from the other. Some slight variance may also result from changes in radiance over the allowed range in the colocated direction angles and from changes in cloud cover between measurements.

The above error sources are mostly random, but there are other sources which may cause bias errors. Another possible source of minor error may be θ-dependent variations in the relative attenuations of visible and shortwave radiances. The effects of all of these errors on the actual relationship should be minimized by the size and heterogeneity of the sample set used here. If it is assumed that a scene varies in structure (i.e., cloud cover and type) in a random fashion over the course of a month, then the rms errors in the monthly mean reflected broadband radiance at that hour are ~2% over land and ~3% over ocean, based on the rms errors of the regression fits and one sample per day during the month.

In the regression analysis of the IR data, a slightly different approach was taken. The atmospheric limb-darkening properties of the two IR spectra are markedly different (MHa). To minimize the effects of limb darkening in the sample set, all window-channel data were normalized to $\theta = 0°$ with the theoretical limb-darkening model given by MHa. Similarly, the N7 LW measurements were normalized with the averaged broadband limb-darkening function $\gamma(\theta)$, derived from the data of Raschke *et al.* (1973) (see MHa). The best correlation coefficients, 0.95 over ocean and land, were found with the normalized data in the following quadratic regression fits:

$$L_{lw} = 25.2 + 10.0BB(T) - 0.200[BB(T)]^2 \quad (3a)$$

over ocean and

$$L_{lw} = 24.0 + 9.43BB(T) - 0.133[BB(T)]^2 \quad (3b)$$

over land as shown in Fig. 2. The symbol BB represents the Planck function evaluated at 11.5 μm. Standard errors of the estimate (SE) for these regression curves, 5% over ocean and 6% over land, indicate that the thermal data are not as sensitive to the error

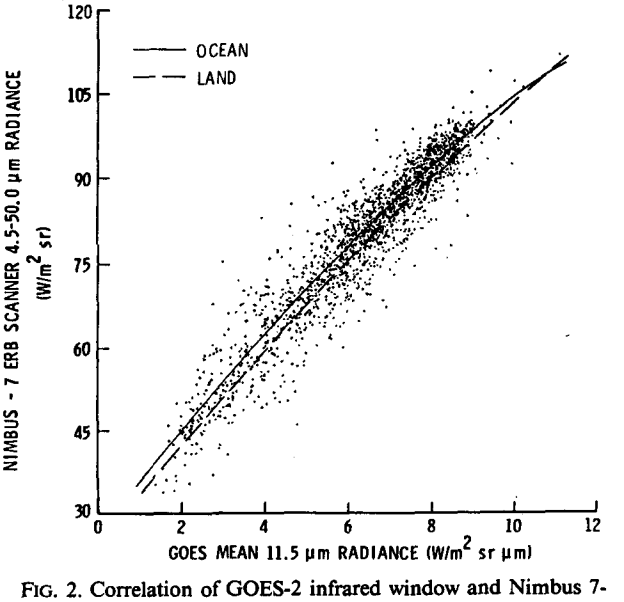

FIG. 2. Correlation of GOES-2 infrared window and Nimbus 7-ERB broadband longwave radiances. Curves represent regression fits.

sources noted earlier and that the IR window spectrum represents the LW spectrum better than the VIS region accounts for the total shortwave spectrum.

Measured IR radiances are usually assumed to have no azimuth angle dependence. Thus, in the integral calculation of M_{lw}, only the anisotropy of L_{lw} due to limb darkening is considered. Therefore,

$$M_{lw} = \int_0^{2\pi} \int_0^{\pi/2} L_{lw} \sin\theta \cos\theta \gamma(\theta) d\theta d\psi.$$

This reduces to

$$M_{lw} = 2.945 L_{lw} \quad (4)$$

for the limb-darkening functions used here.

Plots of M_{lw} versus radiance at 11.5 μm are shown in Fig. 3 for ocean and land, with a regression fit of theoretical broadband LW fluxes and 11.5 μm radiances derived with a radiative transfer routine (Gupta and Tiwari, 1983). The average difference between the empirical and theoretical curves here is 0.2% ± 3.2% over land and 3.0% ± 2.9% over ocean. These differences are within the SE of 4.3% given for the radiative transfer regression fit. The bias over the oceans may result for several reasons. Limb darkening of the higher temperature GOES data may be greater than the average model used here or average atmospheric humidity may have been different than the average of the model atmospheres used in the radiative transfer model (only standard soundings were used).

b. Shortwave bidirectional and directional reflectance models

It is well-known that reflectance anisotropy should be taken into account when computing irradiance (radiant exitance, flux) from radiance. This is especially true for geostationary satellite instruments which are capable of viewing a given location from only one zenith angle. Bidirectional reflectance (BDR) models have been developed by a number of researchers (e.g., Sikula and Vonder Haar, 1972; Raschke *et al.*, 1973) in order to account for anisotropy in the conversion of SW radiance data. These models have been derived from a variety of measured data (e.g., Ruff *et al.*, 1968; Brennan and Bandeen, 1970) taken at various altitudes with several different instruments. Spatial and angular resolution also vary with data source. In order to apply a consistent conversion formula to transform GOES data to flux values and to further examine reflectance anisotropy, a set of models was derived from November 1978 GOES data for ocean and clouds and from a combination of aircraft measurements and GOES data for land surfaces. The development of these models is given in the Appendix.

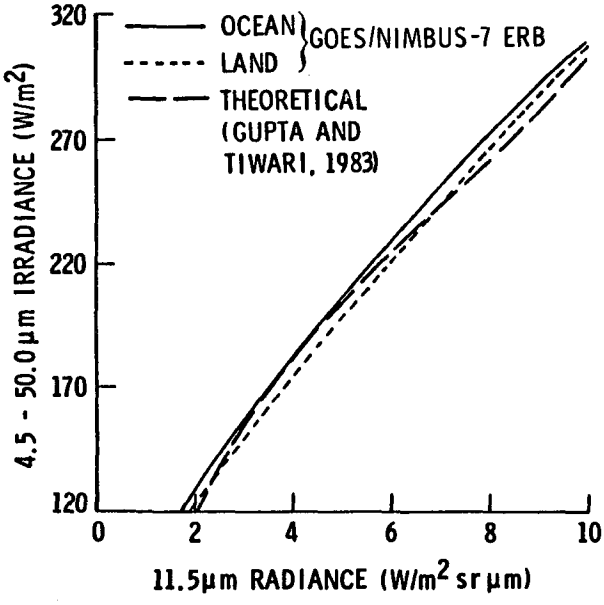

FIG. 3. Empirical and theoretical relationships between broadband radiant exitance and window radiance.

A bidirectional reflectance model consists of anisotropic reflectance correction factors, $\chi(K, \zeta, \theta, \psi)$, which are used to determine the radiant exitance for a given surface type K as

$$M_{sw}(\phi, \lambda, K, \zeta) = \frac{\pi L_{sw}(\phi, \lambda, \zeta, \theta, \psi)}{\chi[K(\phi, \lambda), \zeta, \theta, \psi]}, \quad (5)$$

where ϕ is latitude and λ is longitude. Several examples of $\chi(K, \zeta, \theta, \psi)$ derived in the Appendix are shown in Figs. 4a, b for ocean reflectance at solar zenith angles of 41.4° and 69.5° respectively, in Figs. 4c, d for land reflectance at $\zeta = 40.0°$ and $\zeta = 70.0°$ respectively and in Figs. 4e, f for cloud reflectance at $\zeta = 41.4°$ and $\zeta = 69.5°$ respectively.

Examination of Fig. 4 reveals several fundamental differences in the reflectance patterns over these three surfaces. The contours over the ocean surface show a reflectance minimum centered along the transverse plane ($\psi = 90°$). This minimum area is found at all solar zenith angles. A relative maximum appears in the backscattering direction ($\psi = 0°$) at the horizon for all solar zenith angles. The primary maximum moves with the Sun along the specular point at lower solar zenith angles. Around $\zeta = 50°$, forward scattering from the atmosphere and broadening and shifting of the specular zone from wave effects combine to produce maximum reflectance near the horizon. Since the χ values at $\psi = 180°$ and ζ and $\theta > 50°$ are the results of extrapolations (MHa), they may not be as representative of the average anisotropy as those values at angles where GOES data were available.

Bidirectional reflectance patterns over vegetated land surfaces are considerably different from those over the ocean. Minimum reflectance generally occurs in the forward-scattering direction at low Sun angles. This characteristic and the absence of a specular component may be explained by the shadowing effects and textures of vegetated surfaces. Any terrain feature

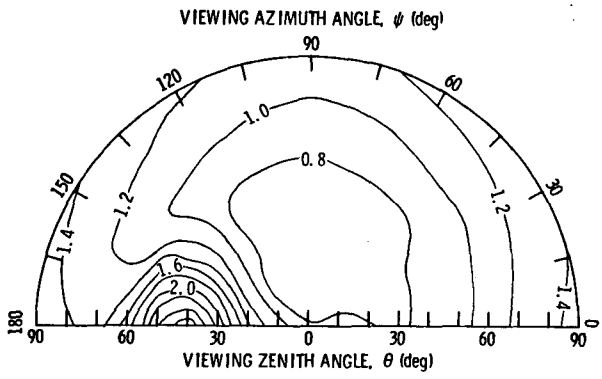

(a) Ocean; sun zenith angle = 41.4°

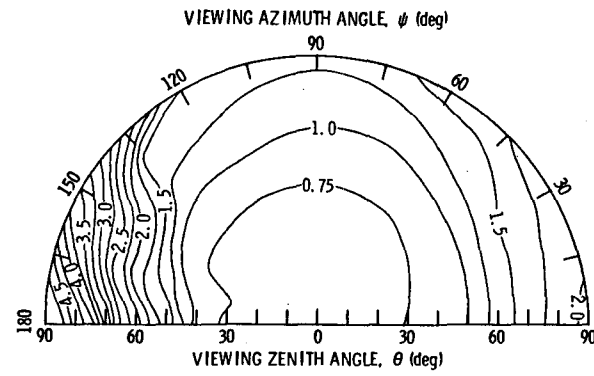

(b) Ocean; sun zenith angle = 69.5°

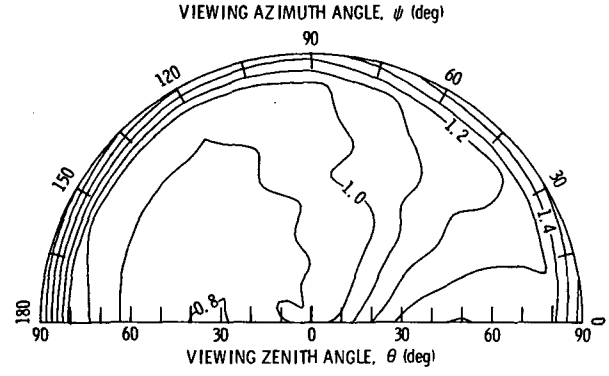

(c) Land; sun zenith angle = 40°

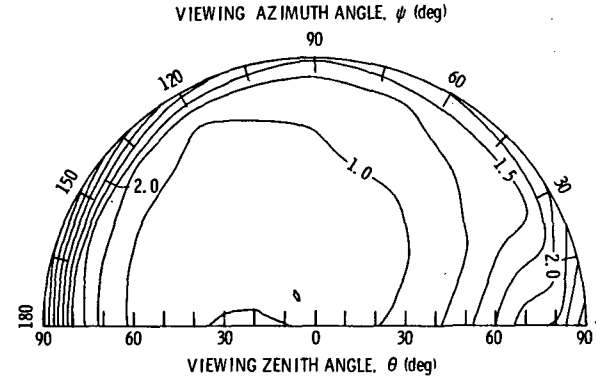

(d) Land; sun zenith angle = 70°

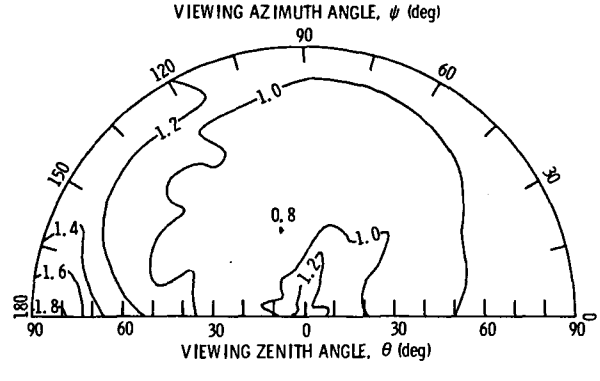

(e) Cloud; sun zenith angle = 41.4°

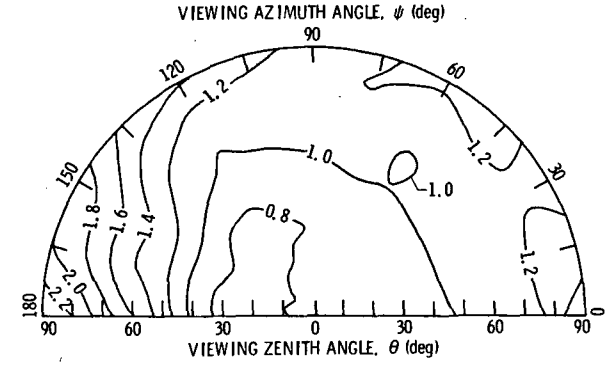

(f) Cloud; sun zenith angle = 69.5°

FIG. 4. Broadband bidirectional reflectance models.

with vertical relief, such as a mountain range, will probably accentuate this shadowing effect. Atmospheric scattering effects tend to cause the high reflectance levels near the horizon. Similar features were observed by Brennan (1969), Paltridge and Sargent (1971) and Eaton (1976) for many different land surfaces. Coulson *et al.* (1965) showed results of SW spectral reflectance measurements over a variety of bare soils and sands. Their curves are very similar to those shown here, suggesting that the bidirectional reflectance model developed for vegetated surfaces may be applicable to bare surfaces. Their data also

indicate that specular reflectance becomes important if the surface is wet.

The bidirectional reflectance properties of clouds appear to be much more complex than those of either water or land. Clouds can cause a variety of reflectance patterns which may be similar to those of water or land surfaces. Layer (infinite) clouds tend to yield strong forward-scattering peaks such as those observed by Brennan and Bandeen (1970) over stratocumulus clouds or by Raschke and Bandeen (1969) for overcast conditions. With the variety of vertical structure observed in cumulus (finite) cloud fields, some shadowing effects similar to land surfaces may be expected. Figs. 4e,f show both of these types of characteristics. Minimum reflectance occurs at $\theta \sim 30°$ at $\psi > 90°$ for both of these cases. The primary maximum is in the forward-scattering direction at high values of θ. Backscattering maxima, evident at low values of θ for $\zeta < 60°$, may be sampling biases resulting from the limited area viewed by GOES-East at those particular angles. At the higher solar zenith angles, the backscattering peak disappears, but the forward-scattering reflectance minima and maxima remain.

The cloud model developed here, representing "average" cloud reflectance characteristics, suggests the possibility of two "average" cloud types: finite and infinite. These two cloud categories have been the subjects of many recent theoretical studies (cf. Welch *et al.*, 1980) which have shown that finite and infinite cloud radiative properties are significantly different. With additional selective analysis of the GOES data, it may be possible to derive two distinct cloud reflectance models.

Directional reflectance is defined as

$$R(\zeta) = M_{sw}(\phi, \lambda, \zeta)/I_0(\zeta), \tag{6}$$

where $I_0 = S\cos(\zeta)$, ϕ is latitude, λ longitude and S the Earth–Sun distance corrected broadband solar irradiance based on a solar constant of 1368 W m^{-2} (Wilson *et al.*, 1981). A general directional reflectance model,

$$\delta(K, \zeta) = \frac{\bar{R}(K, \zeta)}{\bar{R}(K, \zeta = 0°)} = \frac{\bar{M}_{sw}(K, \zeta)}{\bar{M}_{sw}(K, \zeta = 0°)\cos\zeta} \tag{7}$$

can be derived so that the directional reflectance (DR) can be estimated at some arbitrary ζ from a given measurement (Raschke *et al.*, 1973). The overbars in (7) indicate average values. Three types of DR models were derived from the values of $\bar{M}_{sw}(K, \zeta)$ found during the bidirectional reflectance model development.

Figure 5 shows $\delta(K = 1, \zeta)$ for clear ocean. The value of $R(0°)$ is 7.0%. Two other models derived in different ways are also given in Fig. 5 for comparison. The Nimbus 3 model (Raschke *et al.*, 1973) was determined from some aircraft measurements and probably does not include as much atmospheric scattering as a satellite would view. Preuss (1978) computed the subtropical ocean model shown here using radiative transfer calculations and a Fresnel reflecting surface. Many of the differences seen in these models may be due to the effects of wind on the ocean surface. Theoretical results shown by Payne (1972) indicate that sea surface albedo is highly dependent on surface roughness for $\zeta > 60°$. For example, at $\zeta = 80°$ the ocean surface albedo varies from 35% under calm conditions to 19% for an 8 m s^{-1} wind, while there is little variation at $\zeta = 45°$ according to Payne's (1972) Fig. 1.

The land DR model in Fig. 6 is very close to the empirical model shown for comparison. Preuss' (1978) theoretical tropical land model is given since most of the GOES radiances around $\zeta = 0°$ were measured over tropical areas. For the GOES model and the eucalyptus forest data, $R(0°) \approx 15\%$ and $R(0°) \approx 13\%$ respectively. Preuss' (1978) model is the result of radiative transfer computations which calculated planetary DR from reflectance measurements taken close to the ground over green vegetation. Paltridge and Platt's (1976) curve is the planetary DR for only one surface type, while the GOES land model is an average of planetary DR measured over many regions.

One means of determining how well the GOES bidirectional and directional reflectance models together represent land reflectance properties is through comparison of estimates of clear-sky brightness counts with the original values determined by MHa. The original count values D_g were determined by regression on sets of hourly minimum brightness measurements taken over each region. Given the count value at a given hour, it is possible to compute an estimate of the clear-sky brightness $\tilde{D}_g$ at any other hour using (1b) and the land directional and bidirectional reflectance models.

Twenty land regions in the GOES field of view were randomly selected to compare D_g and $\tilde{D}_g$. Using D_g at 1800 GMT and the average November viewing and illumination angles with the appropriate reflec-

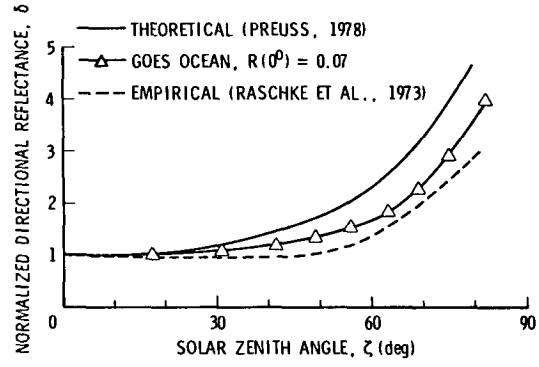

FIG. 5. Ocean directional reflectance models.

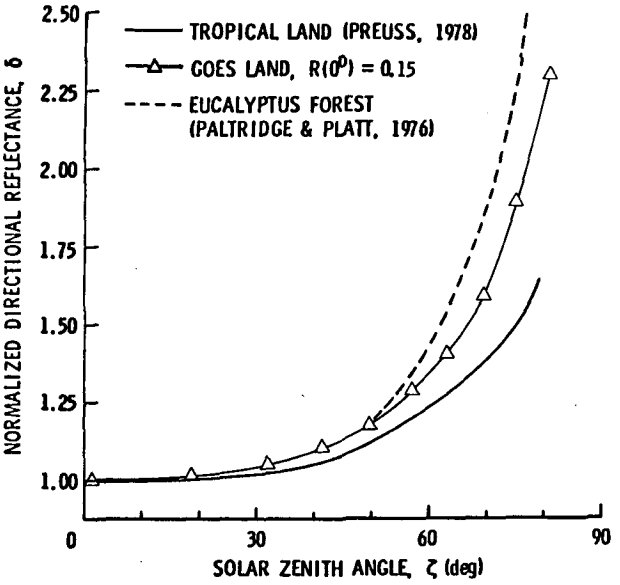

FIG. 6. Land directional reflectance models.

tance models, it was found that the rms error in the estimate $\hat{D}_g$, compared to D_g for a given hour, was 1.0 counts or 8% of the total broadband flux. Clear-sky brightness was also estimated using the land directional reflectance model and Lambertian bidirectional reflectance. For that case the error was 2.0 counts or 19%. The original regression error for all of the GOES regions (MHa) was 0.6 counts (5%). Thus, the BDR and DR models estimate clear-sky brightness from a single measurement nearly as well as the region-specific model does from measurements taken at all daylight hours. The BDR model also improves the precision of hourly reflected flux estimates by more than 100% over a Lambertian model.

The average cloud directional reflectance model is shown in Fig. 7 with both a theoretical and an empirical model for comparison. The GOES cloud model is much like the Nimbus 3 model up to $\zeta = 70°$. At higher solar zenith angles, it approaches the values of the theoretical model, which was derived from an average of cloud reflectance values taken from Liou and Wittman (1979). Their stratocumulus and cumulus reflectances for a vertical liquid water content of 50 g m^{-2} were averaged to yield the curve shown here. More specific cloud models (e.g., overcast, low clouds, etc.) may also be derived from the GOES results for comparisons with other model conditions.

c. *Radiation budget parameters*

The monthly mean net radiation gain in a region is

$$\bar{M}_{\text{net}}(\phi, \lambda) = \bar{I}_0(\phi)[1 - \bar{\alpha}(\phi, \lambda)] - \bar{M}_{\text{lw}}(\phi, \lambda), \quad (8)$$

where ϕ and λ are the latitude and longitude, respectively, at the center of the region. The average incoming solar flux is

$$\bar{I}_0 = \bar{S} \cos\zeta_e, \quad (9)$$

where the average solar constant for the month is

$$\bar{S} = \sum_{i=1}^{30} S_i/30,$$

and the effective November solar zenith angle ζ_e is approximated with

$$\zeta_e = \cos^{-1}[(H - \tan H) \sin\phi \tan\delta_e^*/\pi]. \quad (10)$$

The mean half-day length in radians H is found using the equivalent mean November solar declination, $\delta_e^* = -18.33°$. Monthly mean albedo is

$$\bar{\alpha}(\phi, \lambda) = \frac{\sum_{i=1}^{n_t} \int_{t_i}^{t_{i+1}} \alpha_i(\phi, \lambda, t') \cos\bar{\zeta}(t')dt}{24 \cos\zeta_e}, \quad (11)$$

where the mean albedo for the ith time interval is

$$\alpha_i(\phi, \lambda, t') = \frac{\sum_{j=1}^{30} \sum_{K=1}^{3} R_i(K, \phi, \lambda, t')F_j(K, \phi, \lambda, t') \cos\zeta_j(t')}{\sum_{j=1}^{30} \cos\zeta_j(t') \sum_{K=1}^{3} F_j(K, \phi, \lambda, t')}. \quad (12)$$

The day of the month is given by j, t' is the GMT hour falling in a local time interval, and n_t is the number of time intervals between sunrise and sunset. Mean values of a real cloud fraction, $F(K = 3)$, were reported by MHb.

The last term in (8), the mean LW flux, is

$$\bar{M}_{\text{lw}}(\phi, \lambda) = \frac{\sum_{i=1}^{24} M_{\text{lw}}(\phi, \lambda, t_i')}{24}, \quad (13)$$

where

$$M_{\text{lw}}(\phi, \lambda, t') = \sum_{j=1}^{30} M_{\text{lw},j}(\phi, \lambda, t')/30. \quad (14)$$

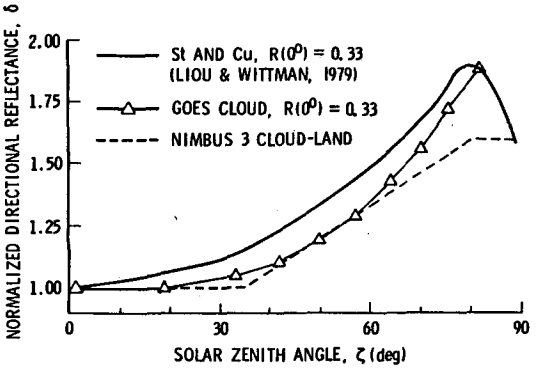

FIG. 7. Cloud directional reflectance models.

Longwave flux may also be partitioned according to scene type (only cloudy or clear) as in (12) except that no $\cos\zeta$ weighting is applicable. Thus, any of the quantities found in (8) through (14) can also be evaluated for just the clear or cloudy portion of the given scene.

Equations (1)–(14) were evaluated using the results of MHa to determine hourly radiation fluxes and the mean radiation balance for each region in the GOES-East study area during November 1978. These data are used as a reference radiation field (a "truth" set) to study the errors in radiation budget caused by the temporal sampling limitations inherent in single Sun-synchronous (SS) satellite measurement systems.

The approach used to evaluate the regional ERB from a simulated SS satellite is similar to the methods used in the past (e.g., Raschke *et al.*, 1973). The following simulated SS measurement system has the additional advantage of knowing the portion of a given measurement due to a particular surface type in the scene. It is assumed that perfect (with respect to the reference) measurements, $M'_{sw}(\phi, \lambda)$ and $M'_{lw}(\phi, \lambda)$, are made each day at t_e and $t_e - 12$, where t_e is the equatorial crossing time of the SS satellite. For simplicity, LW radiant exitance, areal fraction and DR of each surface type measured by the SS satellite at t_e and $t_e - 12$ are assumed to be equal to those same quantities given by the reference data at the nearest GMT hours t'. Thus, the monthly means of the simulated measurements of each quantity at the measurement times are equal to the corresponding monthly means of the reference field at the nearest GMT hours. The simulated, 24-hour monthly means are then computed from the monthly means of the simulated measurements as described below.

Two techniques are used to examine the effects of diurnal cloud variability on limited ERB sampling. The first estimation technique, Method 1, assumes that the estimated monthly mean albedo is

$$\tilde{\alpha}_1(\phi, \lambda) = \alpha(\phi, \lambda, t_e), \tag{15}$$

and the estimated monthly LW flux is

$$\tilde{M}_{lw1}(\phi, \lambda) = [HM_{lw}(\phi, \lambda, t_e) + (\pi - H)M_{lw}(\phi, \lambda, t_e - 12)]/\pi. \tag{16}$$

The estimated net radiation is

$$\tilde{M}_{net1}(\phi, \lambda) = \bar{I}_0(\phi)[1 - \tilde{\alpha}_1(\phi, \lambda)] - \tilde{M}_{lw1}(\phi, \lambda). \tag{17}$$

The errors in these estimates are simply the differences between these values and the corresponding reference values.

Directional reflectance modeling is used in the second estimation technique, Method 2. Mean hourly albedo is

$$\alpha_2(\phi, \lambda, t') = \sum_{K=1}^{3} \bar{R}(K, \phi, \lambda, t_e)\bar{F}(K, \phi, \lambda, t_e)\frac{\delta[K, \zeta(t')]}{\delta[K, \zeta(t_e)]}. \tag{18}$$

These estimated values are then used in (11) to yield $\tilde{\alpha}_2(\phi, \lambda)$. Longwave flux $\tilde{M}_{lw2}$ is the average of the day and night measurements. Net radiation $\tilde{M}_{net2}$ is estimated as in (17). It is implicitly assumed that the scene components (i.e., cloud amount and characteristics) at t_e are constant during the day.

3. Earth radiation budget components from GOES data

This section discusses the various parameters which comprise the reference radiation field. The cloud data used in this "truth" set are described by MHb. The term "clear-sky" refers to the value of a given radiation quantity at the top of the atmosphere over a cloud-free area. The term "ground," designated with the subscript g, is used to indicate a quantity measured relatively close to the Earth's surface. Top-of-the-atmosphere radiative parameters for cloud-covered areas are denoted by the term "cloud."

Examples of the parameters are shown in Fig. 8 for a region at 25.9°S, 68.7°W in South America which is primarily composed of mountainous deserts, but is heavily vegetated near its eastern boundary. The circles in this figure, representing the monthly mean, hourly cloud amount C, show a gradual buildup of convective cloud cover during the daylight hours which begins around 0900 LT (local time) and continues into the night. The dip in C around 1800 LT may be evidence of the decay of the cloudiness or its eastward movement out of the region. The subsequent increase in C to ~20% is due to continuation of the cloud formation process in the middle and upper levels, the movement of middle- and thin, upper-level convective clouds from the north and northwest and the difficulty of distinguishing clouds from mountains with IR data alone (see MHa). The surface elevation in this region varies from ~1000

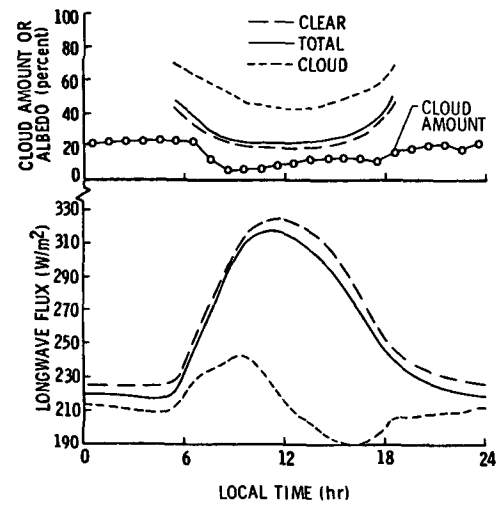

FIG. 8. November 1978 cloud cover and radiative parameters for a region centered at 25.9°S, 68.7°W.

to 6700 m. The decrease in C (mostly midlevel clouds) after sunrise is typical of the diurnal convection patterns seen over much of South America (MHb).

The curves in the top half of the figure describe the average albedo variations over this region. Surface albedo ranges from 19% at noon to 43% at sunrise and is fairly symmetrical about noon. The mean clear-sky albedo is $\bar{\alpha}_s$ = 22%. Cloud albedo varies from 42% at noon to 65% at sunset. Mean cloud albedo is $\bar{\alpha}_c$ = 47%. Total albedo ranges from 21% at 1100 LT to 49% at sunset. The influence of increasing cloud cover during the day may be seen in the slight divergence of the clear-sky and total albedo curves after 1000 LT. Mean total albedo is $\bar{\alpha}$ = 24%. The diurnal ranges in both clear-sky and total LW fluxes, $\Delta M_{\mathrm{lw}s}$ and ΔM_{lw}, respectively, are 100 W m^{-2} over this desert region. A simple average of the minimum and maximum total fluxes would yield 269 W m^{-2}, 12 W m^{-2} higher than the true 24 h average of $\bar{M}_{\mathrm{lw}}$ = 257 W m^{-2}. The mean 24 h clear-sky LW flux is $\bar{M}_{\mathrm{lw}s}$ = 265 W m^{-2}. The large diurnal range in the cloud LW flux, $\Delta M_{\mathrm{lw}c}$ = 54 W m^{-2}, is greater than that found over most other regions in South America. Mean cloud LW irradiance is $\bar{M}_{\mathrm{lw}c}$ = 213 W m^{-2}.

a. Clear-sky parameters

Minimum clear-sky albedo, $\alpha_s(t_{\min}) = \alpha(K < 3, \phi, \lambda, t_{\min})$, is shown in Fig. 9 for November 1978. On the average, $t_{\min}$ = 1200 LT over land and water. Over water, there is little variation in $t_{\min}$ about the mean since its value is dependent on the model shown in Fig. 5. The standard deviation about $t_{\min}$ for land areas is ±1.1 h. This variation is primarily the result of the uncertainties in the minimum brightness values estimated with the regression model of MHa and in the bidirectional reflectance model. In Fig. 8, $\alpha_s(t_{\min})$ = 19% and occurs at noon.

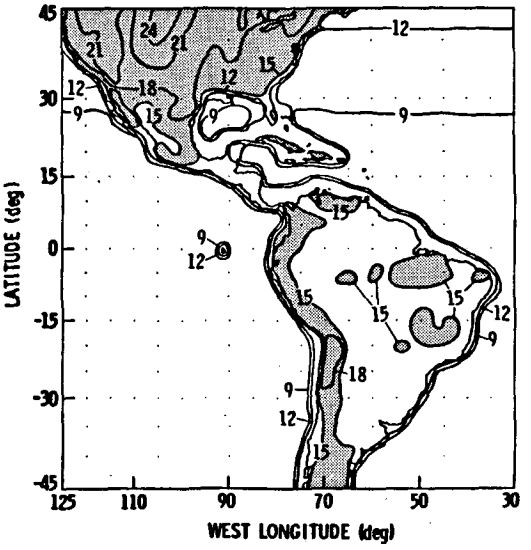

FIG. 9. Minimum clear-sky albedos in percent for November 1978. Shading indicates values > 15%.

The geographical trends of $\alpha_s(t_{\min})$ are very similar to the distribution of ground albedo α_g given by Kung *et al.* (1964), while the magnitudes are greater in some areas and less in other regions. Paltridge and Platt (1976) and Rockwood and Cox (1978) have shown that ground albedo and clear-sky albedo are usually not equal. For typical ranges of atmospheric absorptivity a and transmissivity τ, their models can yield values of α_g which may vary from less than to greater than the corresponding clear-sky albedo. For example, values of α_g computed with the Rockwood and Cox (1978) model for $\alpha_s(t_{\min})$ = 18% range from 15% for a high moisture, low aerosol atmosphere to 30% for a low moisture, high aerosol atmosphere.

Values of α_g given by Kung *et al.* (1964) range from 10 to 16% for the southeastern United States for snow-free areas during winter. Fig. 9 shows $\alpha_s(t_{\min})$ ranging from 15 to 18% for the same area. Over the western United States, Kung *et al.* (1964) reported a range in α_g of 10 to 26%. This may be compared to the values of $\alpha_s(t_{\min})$ in Fig. 9 which vary from 15 to 23% for the same area. It should be noted that some values of α_g for brighter desert areas in North America are much higher than $\alpha_s(t_{\min})$ [e.g., over the Sonoran Desert $\alpha_g \approx 25\%$ and $\alpha_s(t_{\min})$ = 21%]. The more obvious discrepancies may arise for a number of reasons. The minimum reflectance technique (MHa) used to derive $\alpha_s(t_{\min})$ may have missed the brightest area in a region, or some spectral reflectance differences unique to deserts may not have been taken into account with (1b). On the other hand, albedo maps such as that given by Kung *et al.* (1964) are based on the assumption that a given area is covered by a homogeneous surface type (e.g., sand desert or coniferous forest). Vegetation, precipitation, bodies of water and other inhomogeneities may yield an average albedo much different from the surface category albedo. Seasonal variations and spatial resolution differences can also affect the comparisons. The spectral response characteristics of the radiometer used by Kung *et al.* (1964) are also somewhat uncertain. The average values of α_g given by Kung *et al.* (1964) for snow-free land and $\alpha_s(t_{\min})$ in Fig. 9 for North America between 20 and 45°N are 16.5 and 18.8% respectively. This difference could be explained with the Rockwood and Cox (1978) model using τ = 0.74 and a = 0.20, values corresponding to a relatively clear atmosphere.

The average value of $\alpha_s(t_{\min})$ for Central America and the Caribbean islands is 14.9%. This value may be compared with α_g = 10% for the Gulf Coast of Mexico given by Kung *et al.* (1964) and the range of values, 10.8 to 12.5%, for an evergreen tropical forest reported by Pinker *et al.* (1980).

Over South America between 5°N and 45°S, the average value of $\alpha_s(t_{\min})$ is 14.7% which is low compared to a value of 16% computed with the Rockwood

and Cox (1978) model using the November average of α_g = 13.5% found with the data of Hummel and Reck (1979) and the same values of τ and a noted above. The difference between clear-sky and ground albedo at these albedo values, however, should be less for the atmosphere containing more moisture, as may be expected for the atmosphere over much of South America relative to that over North America during November. The largest differences between the present data and the Hummel and Reck (1979) results over South America are found between 10 and 40°S, 40 and 70°W where their value of α_g = 18%. Here $\alpha_s(t_{\min}) \approx 14\%$ and was derived at the 100% sampling level in most regions. This indicates that their assigned values are too high or there are substantial spectral conversion problems for the GOES VIS data in this area.

Minimum clear-sky albedo results for the oceans follow the same pattern given by Hummel and Reck (1979) for November. Differences in the magnitudes of α_g and $\alpha_s(t_{\min})$ may also be explained with the results from the Rockwood and Cox (1978) model for a relatively clear atmosphere. The value of $R(0°)$ = 7.0% over the ocean is similar to the high altitude aircraft measurements over the tropical Atlantic reported by Minnis and Cox (1978). Linear extrapolations of their highest altitude (~230 mb) reflected flux measurements taken in relatively dust-free conditions (days 217–74 and 237–74) yield top-of-the-atmosphere albedos of 7.3% at ζ = 3° and 7.9% at ζ = 17°. Albedos of 6.1% at $\zeta \sim 30°$ and 7.2% at $\zeta \sim 48°$ determined by Brennan and Bandeen (1970) from high altitude aircraft data taken over clear ocean are less than the corresponding values of R over clear ocean.

Average clear-sky albedo $\bar{\alpha}_s$, as found with (11), is shown in Fig. 10. The solar zenith angle dependence

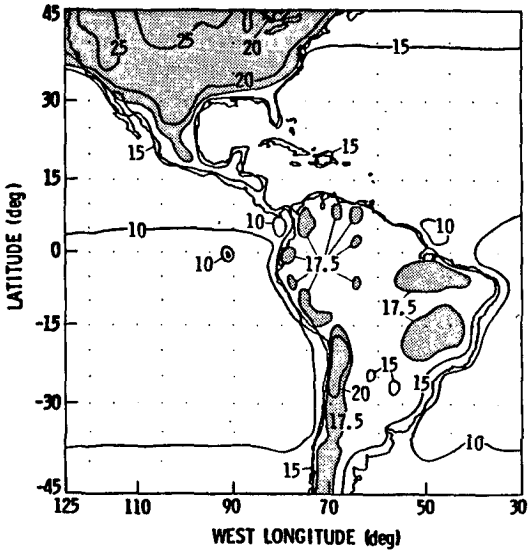

FIG. 10. Average clear-sky albedos in percent for November 1978. Shading indicates values > 17.5%.

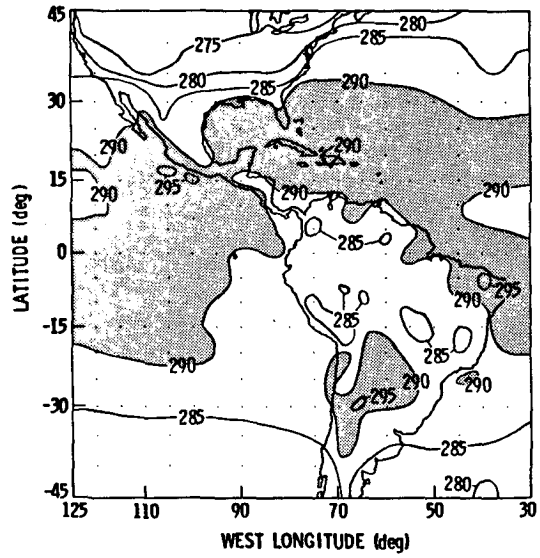

FIG. 11. Average clear-sky temperatures in K for November 1978. Shading indicates values > 290 K.

of directional reflectance results in values of $\bar{\alpha}_s$ which are greater than $\alpha_s(t_{\min})$ by a factor ranging from 1.1 to 1.3. The results in Fig. 10 are generally greater than the average minimum albedos determined by Raschke and Preuss (1979) from Nimbus 3 measurements for June 1969 (not shown). In North America, the primary contour of $\bar{\alpha}_s$ = 20% given by Raschke and Preuss (1979) encompasses less area than the same contour in Fig. 10. The penetration of the $\bar{\alpha}_s$ = 17.5% line deep into northern Mexico is similar to the 15% contour in the Nimbus 3 data. Raschke and Preuss (1979) show a value of $\bar{\alpha}_s$ < 15% for the Brazilian Highlands and the Gran Chaco, which is less than the values of $\bar{\alpha}_s$ (~18%) in Fig. 10. Aside from the Patagonian Desert, the Amazon was the only area in South America with $\bar{\alpha}_s$ > 20% for the Nimbus 3 data. The differences in the results for the two data sets are expected since the Nimbus 3 data were taken during a different time period, with a different instrument, at a lower spatial resolution (250 × 250 km^2 compared to 8 × 8 km^2) and analyzed with different reflectance models. Clouds, especially in convectively active areas such as the Amazon or in areas with frequent cyclonic passage, are more likely to contaminate the lower resolution minimum albedo measurements. The greater values of GOES α_s over North America are probably the result of the higher November solar zenith angles, seasonal vegetation changes and spectral calibration differences. The last factor may be the most important since many of the differences over South America are of similar magnitude and of the same sign as those over North America.

Average November 1978 clear-sky temperatures $\bar{T}_s$ are shown in Fig. 11. This quantity is the 11.5 μm, clear-sky, equivalent blackbody temperature deter-

mined by MHa. The variation in $\bar{T}_s$ appears to be latitudinally dependent, at least in the upper and lower portions of Fig. 11. Over the western United States, the effects of elevated terrain and the position of the mean 750 mb trough (Dickson, 1979) contribute to the dip in $\bar{T}_s$. The relationship between the mean hourly, clear-sky temperature $\bar{T}_s$ and the corresponding shelter air temperature were discussed by MHa. Further comparison of the November 1978 averages of shelter air temperatures over the United States and the corresponding values of $\bar{T}_s$ reveal a mean difference of 5 K with a standard deviation of ±2 K. High humidity and some cloud contamination over South America and the intertropical convergence zone in the Atlantic probably cause the relatively low values of $\bar{T}_s$ over the southern oceans. Drier portions of South America, such as the Gran Chaco and northeastern Brazil, appear as the warmest land areas.

The monthly mean diurnal range of T_s is ΔT_s shown in Fig. 12. Oceanic regions show little diurnal variation in T_s (with a mean diurnal range of 0.8 K), while high elevation desert areas have the highest values of ΔT_s. Most of the heavily vegetated areas outside the Amazon basin have an average diurnal range, $\Delta T_s \approx 7.5$ K. Areas where $\Delta T_s > 10$ K are generally arid or are located at elevations higher than 1 km. The Atacama, Peruvian and Patagonian Deserts and western Gran Chaco and Pampas all have values of $\Delta T_s > 20$ K. The maximum diurnal range of T_s is 38.6 K at 25.9°S and 66.7°W. On the average, the diurnal ranges in the November 1978 shelter air temperatures over the United States are 2 K greater than corresponding values of ΔT_s. The calculation of $\bar{T}_s$ and ΔT_s included those hours which were overcast when the temperature was estimated with linear interpolation. When overcast conditions are eliminated from the averaging, the value of ΔT_s over land may increase by as much as 6 K depending on the number of overcast hours.

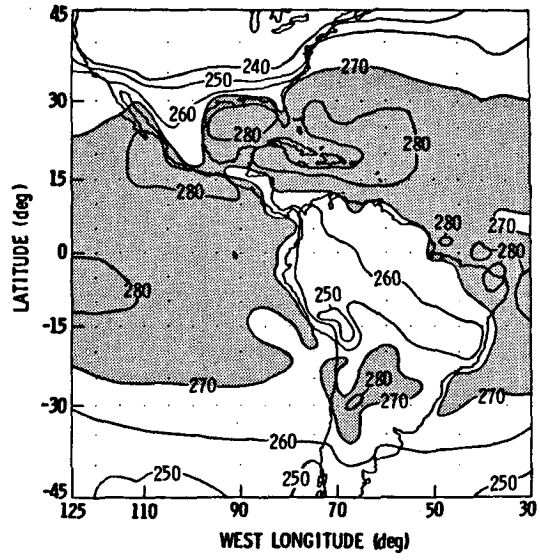

FIG. 13. Average longwave radiant exitances (W m^{-2}) for clear-sky conditions for November 1978. Shading indicates values > 270 W m^{-2}.

Average LW radiant exitances for clear-sky conditions $\bar{M}_{lws}$ are given in Fig. 13. These values follow the same distribution shown in Fig. 12. The corresponding diurnal variations ΔM_{lws} are shown in Fig. 14. Diurnal ranges as high as 100 W m^{-2} are found in the arid, high-altitude regions of the Andes. It is apparent that land surface heating and cooling, especially in desert areas, have an important diurnal effect on the Earth's radiation balance.

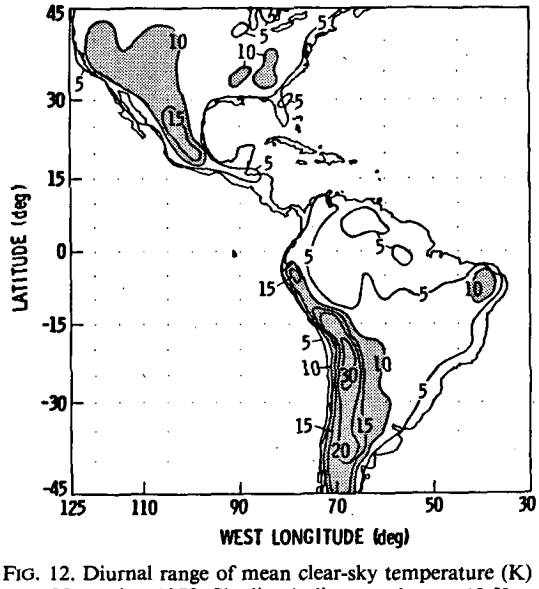

FIG. 12. Diurnal range of mean clear-sky temperature (K) for November 1978. Shading indicates values > 10 K.

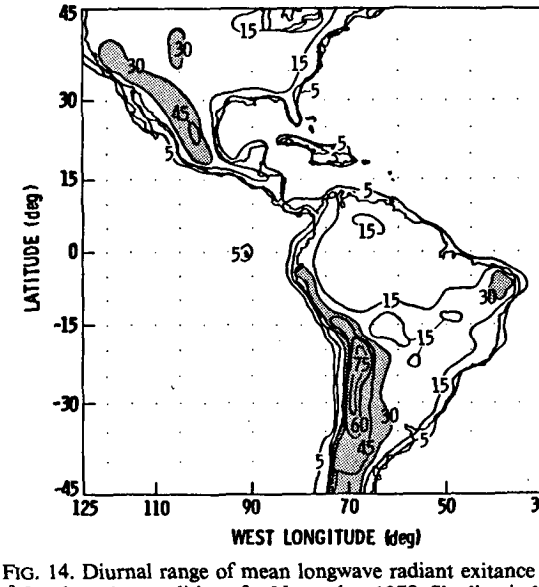

FIG. 14. Diurnal range of mean longwave radiant exitance in W m^{-2} for clear-sky conditions for November 1978. Shading indicates values > 30 W m^{-2}.

b. Cloud parameters

Average regional cloud albedos $\bar{\alpha}_c$ are shown in Fig. 15. Cloud albedo appears to be dependent on both latitude and the type of underlying surface. Highest values of $\bar{\alpha}_c$ are mostly found at the mid-latitudes where the effective solar zenith angle is higher and frontal cloudiness is more common. Clouds over land areas generally have a higher albedo than those over water at the same latitude. This is apparently due to cloudiness over land being higher and thicker than it is over water. This is evident in the values of average cloud temperature given by MHb. If it is assumed that cloud radiative temperature $\bar{T}_c$ is directly dependent on the combination of cloud thickness and cloud altitude, then cloud albedo will be dependent on cloud radiative temperature, since cloud brightness is related to cloud thickness (Kaveney *et al.*, 1977) and cloud height (Park *et al.*, 1974). Fig. 16 shows the ratio of cloud albedos $\bar{\alpha}_c$ over land to those over water at a given latitude as a function of the differences in cloud temperatures over ocean and land. The data in Fig. 16 can be divided into two groups. The lowest ratios in Group 1 (triangles) correspond to the intertropical convergence zone where there is deep convective activity over both land and water. Thus, the low albedo ratios may be due to differences in altitude rather than cloud thickness. The remainder of the triangles primarily represent stratocumulus (Sc) zones over the ocean. For increasing differences in $\bar{T}_c$, increases in $\bar{\alpha}_c$ over land in this area are much less pronounced than in other zones. This may be due to the predominance of low altitude marine stratus and Sc clouds which apparently are as bright as a mix of cloud heights over the ocean at other latitudes relative to the clouds over land. The

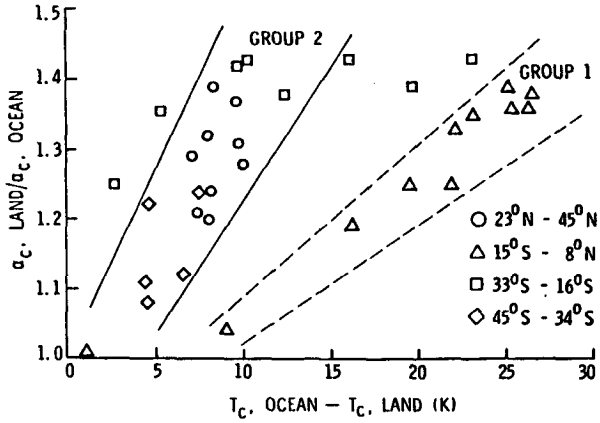

FIG. 16. Comparison of zonal cloud radiative parameters over land and oceans.

Group 2 data in Fig. 16 represent zones where a mix of cloud altitudes is more common over both land and ocean. The squares in Fig. 16 between Groups 1 and 2 represent data from transition zones (16–22°S latitudes). While the differences in $\bar{T}_c$ do not explain all of the differences in cloud albedo over land and water, it is apparent that cloud thickness and brightness, as manifest in $\bar{T}_c$, account for some of the albedo variations. Other factors which may affect these differences include the degree of cloud brokenness, the background albedo, the time of occurrence of highest or thickest cloud cover and the land–ocean differences in cloud droplet size distributions.

Diurnal variations in cloud albedo are dependent on both the predominant type of cloud cover and diurnal changes in average cloudiness. Fig. 7 represents the mean ζ-dependence of α_c for the entire GOES

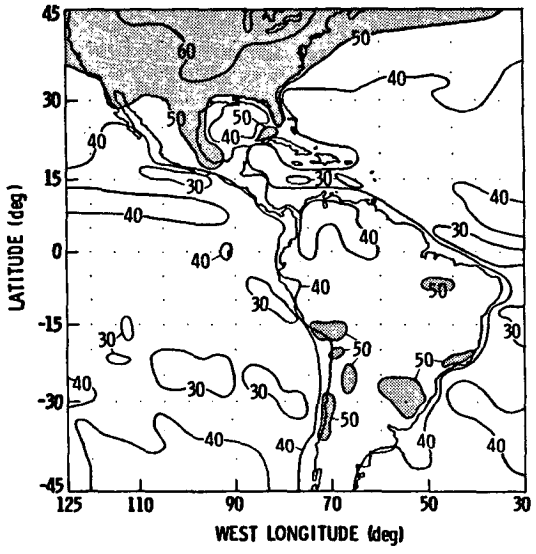

FIG. 15. Average cloud albedo in percent for November 1978. Shading indicates values > 50%.

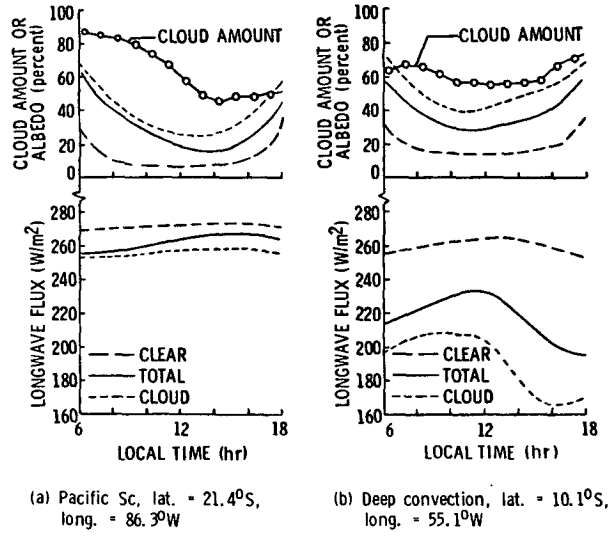

(a) Pacific Sc, lat. = 21.4°S, long. = 86.3°W

(b) Deep convection, lat. = 10.1°S, long. = 55.1°W

FIG. 17. Mean hourly, daytime, regional cloud amounts and radiative parameters for November 1978.

grid for November 1978. On a regional basis, average cloud albedo may change with solar zenith angle in a much different manner. Figs. 17a, b show the daytime variations in cloud cover, α_s, α, α_c, and the corresponding LW fluxes for two tropical regions. Fig. 17a is a typical example of the cloud and radiative parameter variations over the southeastern Pacific Sc regime. During the early morning, the cloud cover is usually rather thick and continuous with α_c (ζ = 77°) = 65%. As the stratus thins out (inferred from the increasing value of M_{lwc}) and breaks up into Sc cells, α_c drops rapidly until noon. For the next few hours, C continues to diminish. Instead of increasing after noon, α_c remains constant until the cloud layer, now mostly broken Sc, stabilizes. Cloud albedo then increases rapidly up to 50% by the time ζ = 76°. The behavior of α_c in this region changes from morning to evening and is quite different from the average $\delta(\zeta)$ shown in Fig. 7. During the morning and afternoon δ (ζ = 77°) = 2.5 and 1.9,respectively, while the average model value is δ (ζ = 77°) = 1.85.

Data are given in Fig. 17b for a region at 10.1°S and 55.1°W where deep convection predominates. The variations in cloudiness and α_c are more complex than found in the previous example. In the early morning, C is composed mostly of diminishing mid-level cloudiness and increasing low clouds (evident in the increasing values of M_{lwc}). Around 1000 LT high clouds are at a minimum, while low clouds are reaching their maximum coverage. Total cloudiness continues to decrease slowly until noon, but the vertical structure changes dramatically. Between 1130 and 1330 LT high-cloud cover more than doubles, α_c rises rapidly from its minimum value at 1030 LT and M_{lwc} drops by 20 W m^{-2}. During the remainder

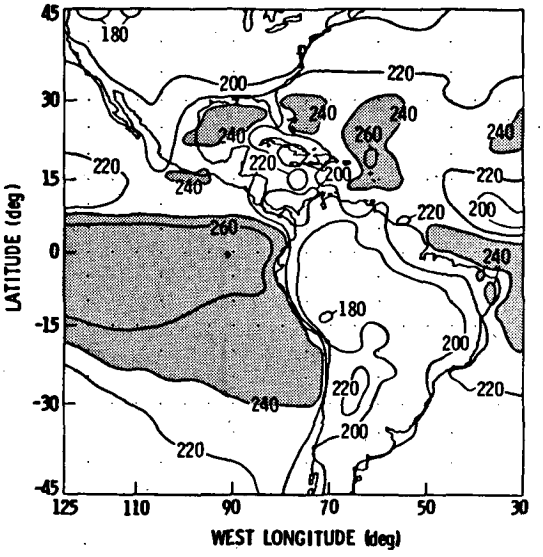

FIG. 18. Mean cloud longwave radiant exitance in W m^{-2} for November 1978. Shading indicates values > 240 W m^{-2}.

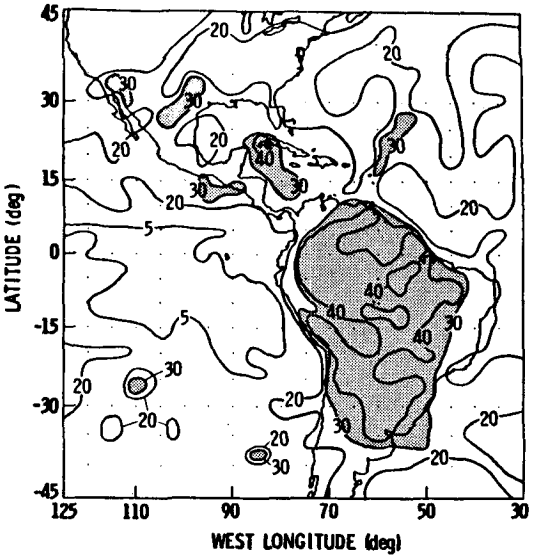

FIG. 19. Diurnal range of mean cloud longwave radiant exitance in W m^{-2} for November 1978. Shading indicates values > 30 W m^{-2}.

of the day, middle- and high-cloud cover continue to increase and low cloudiness decreases. As in the previous example, there are distinct morning and afternoon differences in the nature of the local cloud cover and α_c. In this case, δ (ζ = 77°) = 1.7 and 1.5 during the morning and afternoon respectively.

The average regional cloud LW flux $\bar{M}_{lwc}$ is shown in Fig. 18. This corresponds to the values of $\bar{T}_c$ discussed by MHb. Based on the relationships between cloud albedo and cloud temperature discussed above, it is expected that lowest values of $\bar{M}_{lwc}$ found over the northwestern United States would correspond to the highest values of $\bar{\alpha}_c$. However, the clouds in the midwestern United States are brighter. The higher values of $\bar{\alpha}_c$ over the Plains states may result from clouds which are thicker and more continuous than those to the west.

Figure 19 shows the diurnal range ΔM_{lwc} of M_{lwc}. Here the effects of diurnal variations in the vertical structure of the cloud field are most evident. In areas where ΔM_{lwc} < 15 W m^{-2}, the vertical variations are either absent or tend to cancel each other through various combinations of clouds at different levels. Over parts of South America, where values of ΔM_{lwc} > 40 W m^{-2} are common, deep convective activity is fairly regular on a diurnal basis (MHb).

c. *Total radiation field*

Mean regional albedo as computed with (11) using all three scene categories is shown in Fig. 20. A plot of the corresponding zonal averages is included on the right-hand side of the map. Although this area includes only a portion of the globe, the zonal values of $\bar{\alpha}$ are similar to previous ERB measurements (e.g., Jacobowitz *et al.*, 1979) for the month of November.

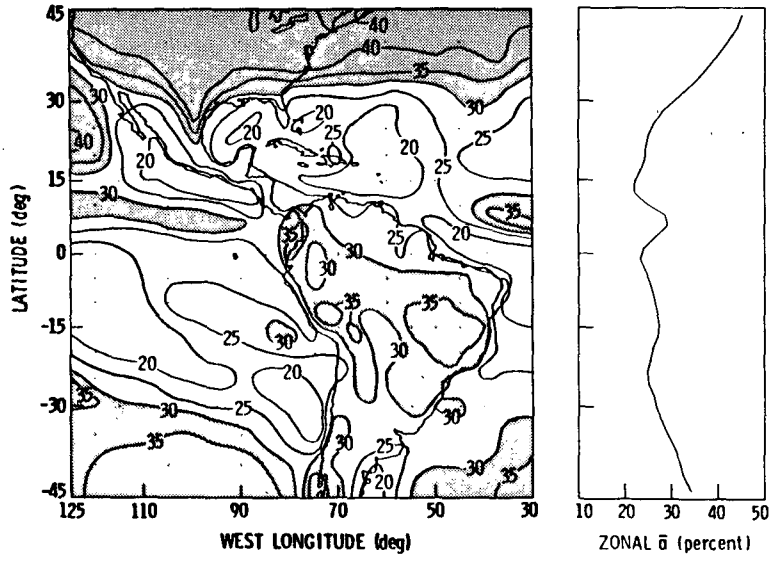

FIG. 20. Mean regional and zonal albedos in percent for November 1978. Shading indicates values > 30%.

Mean total LW flux $\bar{M}_{lw}$ is shown in Fig. 21 for each region. The companion zonal averages are plotted on the right-hand side of the figure. These values are also comparable to the November 1975–76 results given by Jacobowitz *et al.* (1979), except that the present results are somewhat lower south of 30°S. This is consistent with the plots of Winston *et al.* (1979). Their data, while different from the present data in absolute magnitude, show that the outgoing longwave flux between 30 and 45°S is less between 2.5 and 120°W than for all other longitudes during those two years. Fig. 22 shows the diurnal ranges of M_{lw}. Over most ocean areas, the diurnal range is less than 15 W m^{-2} and is primarily due to changes in cloud cover. In continental areas, both surface heating and cloud changes are responsible for the higher values of ΔM_{lw}. North and South American desert areas show relatively large values of ΔM_{lw} which result mostly from surface effects. Over the remainder of South America, deep convective activity causes the large diurnal ranges in outgoing LW flux.

Regional and zonal net radiation data are plotted in Fig. 23. The zonal values are also quite similar to, but slightly less than the results of Jacobowitz *et al.*

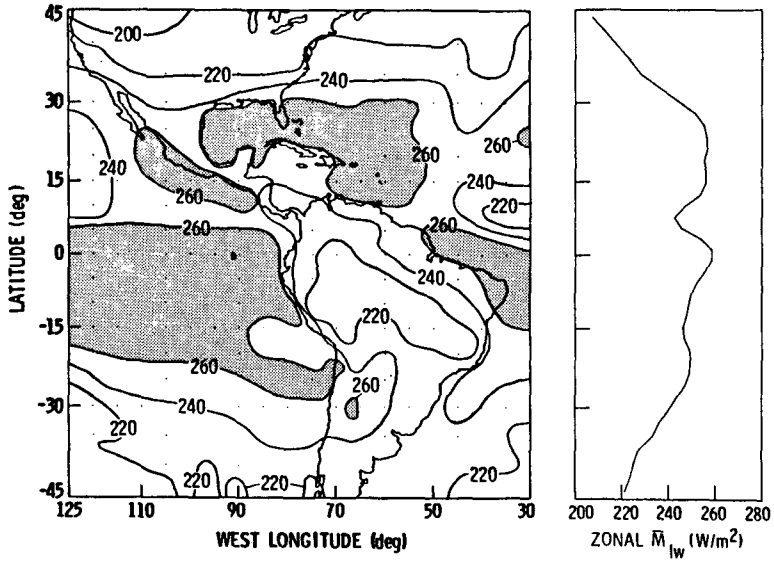

FIG. 21. Mean regional and zonal total longwave flux in W m^{-2} for November 1978. Shading indicates values > 260 W m^{-2}.

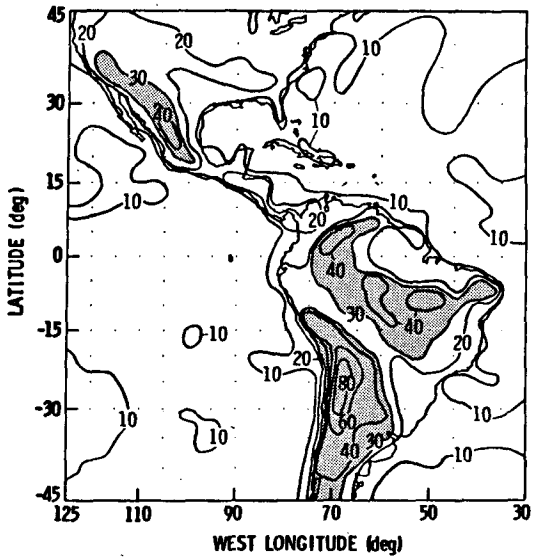

FIG. 22. Diurnal range of mean total longwave flux in W m^{-2} for November 1978. Shading indicates values > 30 W m^{-2}.

(1979). Again, an examination of the data of Winston *et al.* (1979) revealed that, in general, net radiation values between 30 and 45°S for 2.5–120°W are less than the corresponding global zonal average.

The mean radiative parameters for the entire study area are presented in Table 1. These data can be used to estimate the net effect of clouds on the radiation budget in the following manner:

$$\frac{\Delta(\bar{M}_{\text{net}})}{\Delta\bar{C}} = \frac{\Delta\bar{Q}}{\Delta\bar{C}} - \frac{\Delta\bar{M}_{\text{lw}}}{\Delta\bar{C}},$$

where Q is the solar energy absorbed by the system. This can be written as

$$\Delta(\bar{M}_{\text{net}})/\Delta\bar{C} = -\bar{I}_0(\bar{\alpha}_c - \bar{\alpha}_s) - (\bar{M}_{\text{lws}} - \bar{M}_{\text{lwc}})$$
$$= \bar{M}_{\text{netc}} - \bar{M}_{\text{nets}}.$$

For this data set, the change in net radiation due to clouds is −55.0 W m^{-2}, indicating that the albedo effect of clouds is greater than the greenhouse effect. This value, which is close to the global average found theoretically by Schneider (1972), represents 20% of the Earth for one month and covers a variety of climates. A significant portion of this area is dominated by low clouds. Evaluation of the cloud-feedback effect for this large area would require similar analyses of GOES data taken at other seasons to determine if cloud altitude and radiative properties vary in response to changes in cloud amount.

4. Simulation results

The two averaging methods defined in Section 2c were applied to the data discussed in the preceding section. Results of these simulations are summarized in Fig. 24 which shows the average (bias) errors (reference value − simulation estimate) Δ and the regional rms errors RE for each parameter computed with both averaging methods for all 1504 regions. In the case of LW and net radiation, the values of Δ are equivalent to the average error of the entire study area. The values of Δ for albedo are not equal to the average study-area albedo errors since albedo requires energy weighting when averaged.

In almost all cases, Method 2 yields the most accurate results. There are times, however, when both methods show comparable accuracies. For instance, the measured (Method 1) albedo at 0900 and 1500 LT happens to be close to the daily average albedo. In all cases, both methods produce similar

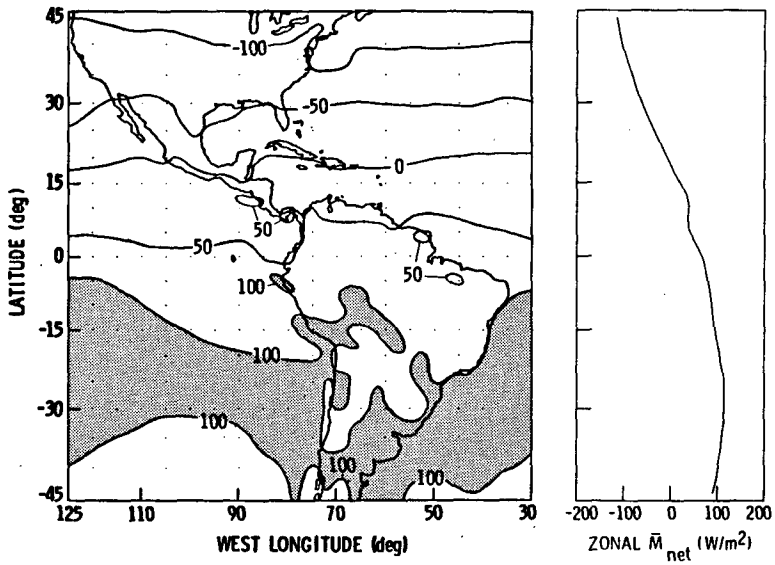

FIG. 23. Regional and zonal net radiation in W m^{-2} for November 1978. Shading indicates values > 100 W m^{-2}.

TABLE 1. Summary of radiation budget parameters for GOES study area, November 1978.

	$\bar{\alpha}$ (%)	$\bar{M}_{lw}$ (W m^{-2})	$\bar{M}_{net}$ (W m^{-2})
Clear sky	12.5	267.3	69.6
Clouds	39.0	220.7	14.6
Total	27.9	242.7	36.6

errors (RE < 3 W m^{-2}) in the LW component. It should be noted that bias errors up to 19 and 16 W m^{-2} are found in some desert areas at t_e = 1200 LT using Method 1 and Method 2 respectively. Because the LW flux follows a predominantly sinusoidal curve during the day (MHa) in these areas, the noon measurement is much higher than the daytime average. The nocturnal curve is much flatter, so the single nighttime measurement represents nighttime conditions relatively well (see, e.g., Fig. 8). The result is an overestimate of $\bar{M}_{lw}$. In portions of the globe where desert conditions are common (e.g., northern Africa), the average error in $\bar{M}_{lw}$ is likely to be greater than that found here for t_e near noon.

The albedo component is highly sensitive to both measurement time and averaging scheme. With the use of DR models (Method 2), however, the maximum RE in albedo is reduced from 11 to 4%; the minimum error is reduced from 2.6 to 1.4%. The smallest bias errors in albedo are found with t_e = 1030 LT and Method 2, while a noon orbit and Method 2 yield the minimum Δ_{net}.

Diurnal variability of cloudiness shows the greatest effects on albedo during early morning and late evening. In a majority of regions, cloudiness reaches a maximum in the early morning (MHb). Therefore, daily albedo is overestimated for measurements taken before noon. The opposite effect occurs for afternoon data since minimum cloud cover is found in many areas in the late afternoon. One reason why the orbits with t_e near noon produce the lowest errors is that average cloud cover is best estimated at those hours.

Another reason is the effect of DR modeling uncertainties. When there is a deviation in local DR behavior from the model DR such as those seen in Fig. 17, the effect on daily albedo is amplified most when the measurement is made near sunrise or sunset. This relative amplification results from two effects. The incident energy in the hours around noon dominates the daily incoming energy, and the deviation from average DR usually increases with time from the measurement. Thus, both the diurnal variability of cloud cover and cloud radiative properties affect the estimates of albedo. To quantify the cloud effect, the simulations were performed again using Method 2, except this time, actual surface albedo was used instead of the model values at each hour. This reduced the relative error by only 5%. Therefore, it may be concluded that 95% of the error in albedo is due to the diurnal variability of cloud cover and cloud radiative properties.

Examination of the net radiation errors reveals some other interesting aspects of measurement time and temporal averaging. It may be concluded from Fig. 24 that there are two equatorial crossing times, $t_e = t_0$, near 0900 and 1500 LT when measurements could be taken and simply averaged (Method 1) to yield $\Delta_{net} \approx 0$, for this particular area and time period. For Method 1, Δ_{net} is very sensitive to t_e, especially near t_0. For example, between 0900 and 1030 LT, Δ_{net} changes by 16 W m^{-2} as it passes through zero. It is probable that t_0 in other areas or time periods is different from t_0 for this data set. Even if it is assumed that t_0 for other situations is within half an hour of the zero points found here, there will still be biases up to at least 5 W m^{-2} for these other conditions.

On the other hand, Method 2 is much less sensitive to t_e on both regional and "global" bases. The average change in Δ_{net} for a given change in t_e is only 2 W m^{-2} per hour compared to 9 W m^{-2} per hour for Method 1. The RE is also less dependent on t_e, ranging from 6 to 14 W m^{-2} relative to the 10 to 40 W m^{-2} range found with Method 1. Thus, it appears

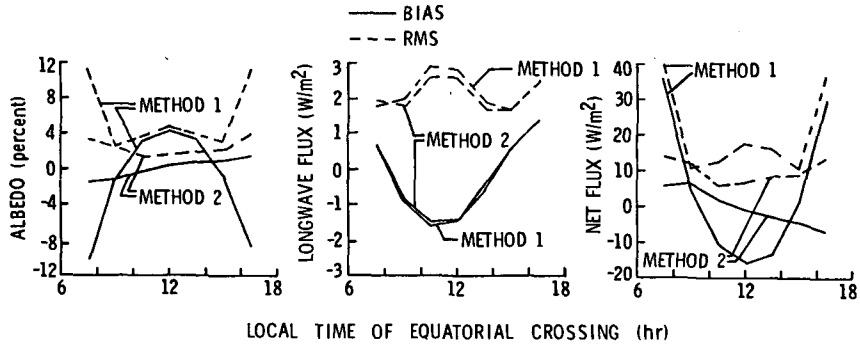

FIG. 24. Regional errors in monthly mean radiation budget parameters from simulations of single Sun-synchronous satellite measurements of the November 1978 GOES-derived radiation field as functions of satellite equatorial crossing times.

that Method 2 will always provide the most reliable results regardless of t_e. Further improvements in ERB estimation techniques beyond Method 2 could possibly be obtained with more localized DR models. The surest means to increase the accuracies of both regional and global ERB estimates is through improved temporal sampling of the diurnally varying radiation field. This approach is already being realized in the development of the multiple satellite Earth Radiation Budget Experiment (ERBE) to be flown in the mid-1980s (Woerner *et al.*, 1978).

It should be emphasized that while the present study encompasses several different climate regions and cloud conditions, the data set is not random in either temporal or spatial coverage. The types of cloud variability and radiative effects in other locales or during other time periods remain for future research. The results discussed in this section are also representative of the most ideal cases. That is, it was assumed that the radiation parameters were measured and interpreted perfectly at the given equatorial crossing times. In any ERB measurement system there will be numerous other error sources such as instrument accuracy, data dropouts, scene identification and bidirectional reflectance modeling.

There is also some error in the Method 2 results due to the use of monthly average values in the averaging scheme. The usual process is to produce a daily value from each measurement, then compute the monthly average. Additional research efforts should use the actual daily averaging method, especially when multiple satellite systems are considered.

5. Summary and concluding remarks

An hourly broadband radiation field was developed from November 1978 GOES-East VIS and IR window data, derived cloud data and empirical spectral transfer functions. This radiation data set was then used to examine some of the effects of the diurnal variability of cloud and surface radiative parameters on estimates of the Earth's radiation budget using measurements taken from Sun-synchronous satellites.

The spectral transfer functions were derived from GOES VIS and IR data correlated with Nimbus 7 ERB shortwave and longwave radiance measurements over ocean and land surfaces. The IR window channel appears to yield more accurate broadband LW radiance estimates than estimates of SW flux derived from VIS channel data. Radiances measured in narrow spectral intervals will obviously not yield broadband radiance fields as accurate as those measured with equal precision in broad spectral intervals. The correlations and comparisons given here, however, indicate that the converted narrowband data are quite adequate for determining relative changes in the Earth's radiation budget and, possibly, the magnitudes of the components of the radiation budget on an average basis. In any event, until broadband instrumentation is employed to sample the ERB at a higher temporal resolution, narrowband data taken by geostationary satellites are the best measurements available to study the diurnal cycle of the ERB.

Three bidirectional and directional reflectance models were derived from the GOES cloud and spectrally-corrected, VIS count data. These were used to account for the reflectance anisotropy of the major scene categories: ocean, land and clouds. It was found that the anisotropic reflectance characteristics of the three categories are generally quite distinct. The solar zenith angle dependence of directional reflectance is different for each scene type and perhaps dependent on the value of directional reflectance under an overhead sun. Between 0 and 80° solar zenith angles, the average directional reflectance varies by factors of 4.2, 2.2 and 1.8 for ocean, land and clouds respectively. Regionally averaged data indicate that the ζ dependence of cloud albedo is variable from region to region. This variability is primarily due to regional differences in cloud type and cloud diurnal cycles.

Clear-sky albedo was also estimated for each region. North American regions have an average midday albedo of 18.8%. Average South American albedo near local noon is about 14.7%. Diurnal variations in clear-sky longwave radiant exitance ranged from 2 to 100 W m^{-2}. The diurnal range of average LW flux from clouds reached 50 W m^{-2} in some regions where deep cumulus convection was prevalent.

Average clear-sky albedo and LW flux for the entire GOES study area were 12.5% and 267.3 W m^{-2} respectively. Over clouds, the average albedo and LW flux were 39.0% and 220.7 W m^{-2}. The combination of clear-sky and cloudy areas yielded an average albedo of 27.9% and LW radiant exitance of 242.7 W m^{-2} for the area bounded by 45°N and 45°S latitude and 30 and 125°W longitude. These results indicate that the clouds produced a net cooling effect of -55.0 W m^{-2} for this area and time period.

Radiation budgets were estimated from simulated Sun-synchronous satellite samplings to study the effects of temporal averaging techniques, equatorial crossing time and the diurnal variability of the radiation field components on errors in the resultant radiation budgets. It was found that average LW radiant exitance could be estimated with an accuracy of less than 3 W m^{-2} for any given equatorial crossing time t_e, using either a simple or daylight-weighted average of the daytime and nighttime measurements.

Estimates of albedo and net radiation are much more sensitive to averaging technique and time of measurement than the LW flux. When directional reflectance (DR) models are not applied to the albedo measurements (Method 1), the errors in mean albedo and net radiation are usually much greater than when the DR models are applied (Method 2). It is concluded that DR models should always be used when estimating daily albedo from a single satellite measure-

ment. The most accurate results are found when t_e is within 1.5 hours of local noon. Since most of the regional error is due to the diurnal variability of cloud cover and cloud radiative properties, it is felt that further reduction of the regional error is possible through several means. One is to develop and apply more specific climatological cloud and cloud radiative parameter models to Sun-synchronous satellite albedo measurements. The other means, which could be used in the development of the first suggestion, is to sample the radiation field more often and at more local times with multiple satellites.

This particular data set shows that there is a significant diurnal cycle in the Earth's radiation field which is dependent on the diurnal variations of cloud cover, its radiative properties and, to a lesser extent, surface radiative properties. The effects of these diurnal variations can lead to substantial errors (as high as 14 W m^{-2} for Method 2) in the estimates of regional radiation budgets computed with Sun-synchronous satellite data. Much additional research utilizing data taken over other regions and during other time periods is required to determine how well the present results represent global conditions.

Acknowledgments. The contributions of Messrs. G. G. Gibson, F. M. Denn, I. J. Walker and P. G. Renfroe of Kentron International, Inc. to the analysis and graphical presentation of this data set are gratefully acknowledged. We would like to thank the Nimbus 7 ERB Science Team for the opportunity to use data from their experiment. Computer programming support provided by Ms. G. Lobo of Computer Sciences Corporation has been essential to the execution of this study. The efforts of Ms. J. Cridlin of the NASA Langley Research Center in preparing the manuscript are deeply appreciated.

APPENDIX

Bidirectional Reflectance Model Development

Reflectance anisotropy depends on a great number of variables which are functions of surface type and atmospheric conditions. It is virtually impossible to account for all of these variables for each surface type. By deriving average bidirectional reflectance (BDR) values for some basic surface categories, it should be possible to at least account for some of the anisotropic effects. The remainder of the effects should be diminished further by averaging data interpreted with the general BDR models over longer time periods. This section describes the development of BDR models for ocean, land and cloud surfaces.

Shortwave radiant exitance, or flux, is defined here as

$$M(\phi, \lambda, \zeta) = \int_0^{2\pi} \int_0^{\pi/2} L_{sw}(\phi, \lambda, \zeta, \theta, \psi) \cos\theta \sin\theta d\theta d\psi. \quad \text{(A1)}$$

The symbols ϕ and λ refer to latitude and longitude, respectively, and ζ, θ and ψ, the solar zenith, satellite zenith and relative azimuth angles respectively. The forward scattering direction is at $\psi = 180°$. For a diffuse surface, (A1) reduces to

$$M_{sw}(\phi, \lambda, \zeta) = \pi L_{sw}(\phi, \lambda, \zeta). \quad \text{(A2)}$$

If radiances are measured from all directions, then (A1) may be solved and the equivalent Lambertian radiance, $L_{sw}(\phi, \lambda, \zeta)$, can be determined from (A2). The ratio

$$\chi(\phi, \lambda, \zeta, \theta, \psi) = \frac{L_{sw}(\phi, \lambda, \zeta, \theta, \psi)}{L_{sw}(\phi, \lambda, \zeta)} \quad \text{(A3)}$$

defines the relative anisotropy of a given measured radiance and is called the anisotropic reflectance correction factor. A set of these correction factors for all angles constitutes a BDR model and can be used to convert a value of L_{sw} directly to M_{sw}, i.e.,

$$M_{sw}(\phi, \lambda, \zeta) = \frac{\pi L_{sw}(\phi, \lambda, \zeta, \theta, \psi)}{\chi(\phi, \lambda, \zeta, \theta, \psi)}. \quad \text{(A4)}$$

If it is assumed that a BDR model exists for each surface category K and that the radiance $\bar{L}_{sw}(K, \zeta, \theta, \psi)$ is defined as the average of all radiances measured at all locations having surface type K, then the coordinates, ϕ and λ, can be replaced by K in (A1)–(A4). This surface category model then is

$$\chi(K, \zeta, \theta, \psi) = \frac{\pi \bar{L}_{sw}(K, \zeta, \theta, \psi)}{M_{sw}(K, \zeta)}. \quad \text{(A5)}$$

The shortwave BDR model for clear ocean, $K = 1$, was derived from the GOES visible count data used by MHa to develop a visible channel ocean model. The minimum count values, D_{min} ($K = 1$, ζ, θ, ψ), in each angular bin were converted to values of $\bar{L}_{sw}(1, \zeta, \theta, \psi)$ with Eqs. (1) and (2). Eq. (A1) was solved numerically with these radiances, and broadband values of χ ($K = 1$, ζ, θ, ψ) were determined with (A5). Plots and discussion of these models are presented in the main text.

A different approach was taken to develop a BDR model for land, $K = 2$. The number of land regions viewed by GOES is rather limited, and the variation in land types is large. Kriebel (1978) derived biconical reflectance factors from radiance measurements taken in several wavelengths over various surface types from an aircraft with a resolution of 10° in ζ and θ, and 30° in ψ. His data taken over a savanna, a coniferous forest and pasture land (designated by $k = 1$, 2 or 3, respectively) at 0.606 and 0.866 μm were combined and calibrated with the GOES results to generate a land BDR model. The procedure, described below, attempts to account for the limited land-sampling capabilities of the GOES with the aid of Kriebel's (1978) data.

It was assumed that the visible bidirectional reflectance for any land surface is

$$\rho_L(\zeta, \theta, \psi) = \{\sum_{k=1}^{3} F\chi_6(\zeta, \theta, \psi, k) + (1 - F)\chi_8(\zeta, \theta, \psi, k)\}/3, \quad \text{(A6)}$$

where $F = w_6R_6/(w_6R_6 + w_8R_8)$ and R_6 and R_8 are the directional reflectances in the 0.606 and 0.866 μm spectral regions. The terms w_6 and w_8 are weighting factors with values of 0.724 and 0.276 respectively. These values are based on a rough partitioning of incident solar radiation, where the lower wavelength accounts for the 0.55–0.68 μm region and 0.866 μm is assumed to be representative of the 0.68–0.75 μm interval. The value of 0.68 μm was found by assuming that the spacing of the spectra used by Kriebel (1978) was such that the half-power wavelengths of each channel were contiguous with neighboring channels. The spectral anisotropic reflectance correction factors, χ_6 and χ_8, for each land type were computed with (A1), (A2) and (A3) using the appropriate biconical reflectance factors from Kriebel (1978) instead of radiances.

The reflectance factors derived with (A6) were used to compute a normalized visible BDR model, $\chi_L(\zeta, \theta, \psi)$, for vegetated land surfaces with equations equivalent to (A1)–(A3). This model is the land equivalent of $\chi_v(\zeta, \theta, \psi)$, the visible ocean BDR model. These factors were then converted to broadband radiances. This conversion utilized the GOES data in the following manner. A pair of satellite zenith and relative azimuth angles was selected based on the maximum number of land regions viewed by GOES at those angles over all solar zenith angles. This pair is defined by $\theta = 40° \pm 5°$ and $\psi = 45° \pm 15°$. All monthly mean, squared, clear-sky brightness counts, $D_g^2(\phi, \lambda, \zeta, 40°, 45°)$, determined by MHa for land surfaces were averaged for each 0.1° interval of cosζ. These averages, $D_g^2(\zeta, 40°, 45°)$, are shown in Fig. A1 with a smoothed curve. The D^2 intercept was found through iteration on (A4) with the assumption that minimum reflectance occurs at $\zeta = 0°$. Visible count values at other angles,

$$D_g^2(\zeta, \theta, \psi) = D_g^2(\zeta, 40°, 45°)\frac{\chi_L(\zeta, \theta, \psi)}{\chi_L(\zeta, 40°, 45°)}, \quad \text{(A7)}$$

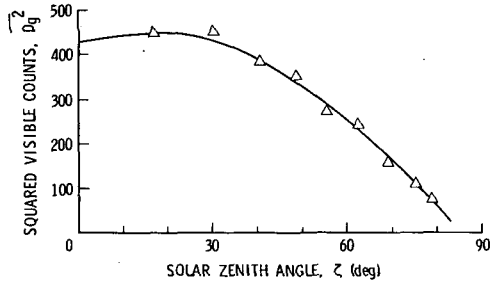

FIG. A1. Monthly mean clear-sky VIS brightness counts for land surfaces used in reflectance model calibration.

were computed and converted to L_{sw} $(K = 2, \zeta, \theta, \psi)$ using (1) and (2). Radiant exitance, M_{sw} $(K = 2, \zeta)$, was determined with (A1) and used to derive the land broadband anisotropic reflectance correction factors, χ $(K = 2, \zeta, \theta, \psi)$, with (A2) and (A3). Some contours of this BDR model are shown in Fig. 4.

A general BDR model for clouds, $K = 3$, was derived directly from the November 1978 GOES cloud data. Visible cloud brightness values and cloud amount C were computed by MHa for each region in the GOES grid for $\zeta < 82°$ between the hours 1200 and 2300 GMT. This cloud brightness is

$$D_c^2 = D_c^2(\phi, \lambda, \zeta, \theta, \psi).$$

Each of these values was converted to broadband radiance, L_{sw} $(K = 3, \phi, \lambda, \zeta, \theta, \psi)$, with (A1). The average cloud radiance for each angular bin defined in MHa was computed as follows:

$$\bar{L}_{sw}(K = 3, \zeta, \theta, \psi) = \frac{\sum_{i=1}^{n} L_{sw}(K = 3, \phi, \lambda, \zeta, \theta, \psi)C_i(\phi, \lambda, \zeta)}{\sum_{i=1}^{n} C_i(\phi, \lambda, \zeta)}, \quad \text{(A8)}$$

where n is the number of measurements in the angular bin for cloud amounts greater than 10%. Empty bins were filled with bilinear interpolation and extrapolation. Anisotropic reflectance correction factors, χ $(K = 3, \zeta, \theta, \psi)$, were then computed with (A1), (A2) and (A4) using the values of $\bar{L}_{sw}$ from (A8). Some portions of this model are shown in Fig. 4.

REFERENCES

Brennan, B., 1969: Bidirectional reflectance measurements from an aircraft over natural Earth surfaces. NASA TM-X-63564, 84 pp. [NTIS-N69-28454].

——, and W. R. Bandeen, 1970: Anisotropic reflectance characteristics of natural Earth surfaces. *Appl. Opt.*, **9**, 405–412.

Coulson, K. L., G. M. Bouricius and E. L. Gray, 1965: Optical reflection properties of natural surfaces. *J. Geophys. Res.*, **70**, 4601–4611.

Dickson, R. R., 1979: Weather and circulation of November 1978. *Mon. Wea. Rev.*, **107**, 219–224.

Eaton, F. D., 1976: Albedo of the Earth's surface—A comparison of measurements taken on the ground and from flying platforms. Ph.D. thesis, Utah State University, Logan, 169 pp. [NTIS-N77-13583].

Gruber, A., and J. S. Winston, 1978: Earth-atmosphere radiative heating based on NOAA scanning radiometer measurements. *Bull. Amer. Meteor. Soc.*, **59**, 1570–1573.

Gupta, S. K., and S. N. Tiwari, 1983: Estimation of longwave flux from radiance measurements in the atmospheric window region. NASA CR 172185, 19 pp. [NTIS-83N 32796].

Hummel, J. R., and R. A. Reck, 1979: A global surface albedo model. *J. Appl. Meteor.*, **18**, 239–253.

Jacobowitz, H., W. L. Smith, H. B. Howell, F. W. Nagle and J. R. Hickey, 1979: The first 18 months of planetary radiation budget measurements from the Nimbus 6 ERB experiment. *J. Atmos. Sci.*, **36**, 501–507.

Kaveney, W. J., R. G. Feddes and K. Liou, 1977: Statistical inference of cloud thickness from NOAA 4 scanning radiometer dasta. *Mon. Wea. Rev.*, **105**, 99–107.

Kriebel, K. T., 1978: Measured spectral bidirectional reflection properties of vegetated surfaces. *Appl. Opt.*, **17**, 253–259.

Kung, E. C., R. A. Bryson and D. H. Lenschow, 1964: Study of a continental surface albedo on the basis of flight measurements and structure of the Earth's surface cover over North America. *Mon. Wea. Rev.*, **92**, 543–564.

Liou, K., and G. D. Wittman, 1979: Parameterization of the radiative properties of clouds. *J. Atmos. Sci.*, **36**, 1261–1273.

Minnis, P., and S. K. Cox, 1978: Magnitude of the radiative effects of the Saharan dust layer. Atmos. Sci. Paper No. 283, Colorado State University, Ft. Collins, 111 pp. [ISSN 0067–0340].

——, and E. F. Harrison, 1984a: Diurnal variability of regional cloud and clear-sky radiative parameters derived from GOES data. Part I: Analysis method. *J. Climate Appl. Meteor.*, **23**, 993–1011.

——, and ——, 1984b: Diurnal variability of regional cloud and clear-sky radiative parameters derived from GOES data. Part II: November 1978 cloud distributions. *J. Climate Appl. Meteor.*, **23**, 1012–1031.

NASA, 1971: Earth albedo and emitted radiation. NASA SP-8067, 44 pp. [NTIS-N71-33104].

Paltridge, G. W., and S. L. Sargent, 1971: Solar and thermal radiation measurements to 32 km at low solar elevations. *J. Atmos. Sci.*, **28**, 242–253.

——, and C. M. R. Platt, 1976: *Radiative Processes in Meteorology and Climatology.* Elsevier, 318 pp.

Park, S., D. N. Sikdar and V. E. Suomi, 1974: Correlation between cloud thickness and brightness using Nimbus 4 THIR data (11.5-μm channel) and ATS 3 digital data. *J. Appl. Meteor.*, **13**, 402–410.

Payne, R. E., 1972: Albedo of the sea surface. *J. Atmos. Sci.*, **29**, 959–970.

Pinker, R. T., O. E. Thompson and T. F. Eck, 1980: The energy balance of a tropical evergreen forest. *J. Appl. Meteor.*, **19**, 1341–1350.

Preuss, H. J., 1978: Bestimmung der Kurzwelligen Strahlungsbilanz am Boden aus Messungen des Satelliten Nimbus 3, 72 pp. [Diplomarbeit, available from the Inst. fur Geophysik und Meteor., Koln, FGR.]

Raschke, E., and W. R. Bandeen, 1969: Beobachtungen der Reflexionseigenschaften des Systems Erde-Atmosphare und der Bewolkung uber dem aquatorialen Pazifik von einem synchronen Satelliten aus. *Ann. Meteor.*, **4**, 200–205.

——, and H. J. Preuss, 1979: The determination of the solar radiation budget at the Earth's surface from satellite measurements. *Meteor. Rundsch.*, **32**, 18–28.

——, T. H. Vonder Haar, M. Pasternak and W. R. Bandeen, 1973: The radiation balance of the Earth–atmosphere system from Nimbus 3 radiation measurements. NASA TN D-7249, 73 pp. [NTIS-N73-21702].

Rockwood, A. A., and S. K. Cox, 1978: Satellite inferred surface albedo over northwestern Africa. *J. Atmos. Sci.*, **35**, 513–522.

Ruff, I., R. Koffler, S. Fritz, J. S. Winston and P. K. Rao, 1968: Angular distribution of solar radiation reflected from clouds as determined from TIROS IV radiometer measurements. *J. Atmos. Sci.*, **25**, 323–332.

Schneider, S. H., 1972: Cloudiness as a global feedback mechanism: The effects of the radiation balance and surface temperatures in cloudiness. *J. Atmos. Sci.*, **29**, 1413–1422.

Sikula, G. S., and T. H. Vonder Haar, 1972: Very short range local area weather forecasting using measurements from geosynchronous meteorological satellites. AFCRL-72-0260, Bedford, MA, 73 pp. [NTIS-AD-744098].

Vonder Haar, T. H., 1968: Variations of the Earth's radiation budget. Ph.D. thesis, University of Wisconsin, Madison, 118 pp. [NTIS-N69-19231].

——, G. G. Campbell, E. A. Smith, A. Arking, K. Coulson, J. Hickey, F. House, A. Ingersoll, H. Jacobowitz, L. Smith and L. Stowe, 1981: Measurements of the Earth's radiation budget from satellites during the First GARP Global Experiment. *Adv. Space Res.*, **1**, 285–297.

Welch, R. M., S. K. Cox and J. M. Davis, 1980: *Solar Radiation and Clouds. Meteor. Monogr.*, No. 39, Amer. Meteor. Soc., 96 pp.

Wilson, R. C., S. Gulkis, M. Janssen, H. S. Hudson and G. A. Chapman, 1981: Observations of solar irradiance variability. *Science*, **211**, 700–703.

Winston, J. S., A. Gruber, T. I. Gray, Jr., M. S. Varnadore, C. L. Earnest and L. P. Mannello, 1979: Earth atmosphere radiation budget analyses derived from NOAA satellite data June 1974–February 1978. Vols. 1 and 2. NOAA-NESS, Washington, DC, 680 pp. [NTIS-N79-31862].

Woerner, C. V., J. E. Cooper and E. F. Harrison, 1978: The Earth radiation budget satellite system for climate research. *Remote Sounding of the Atmosphere from Space, Vol. 4*, H. J. Bolle, Ed., 201–215.